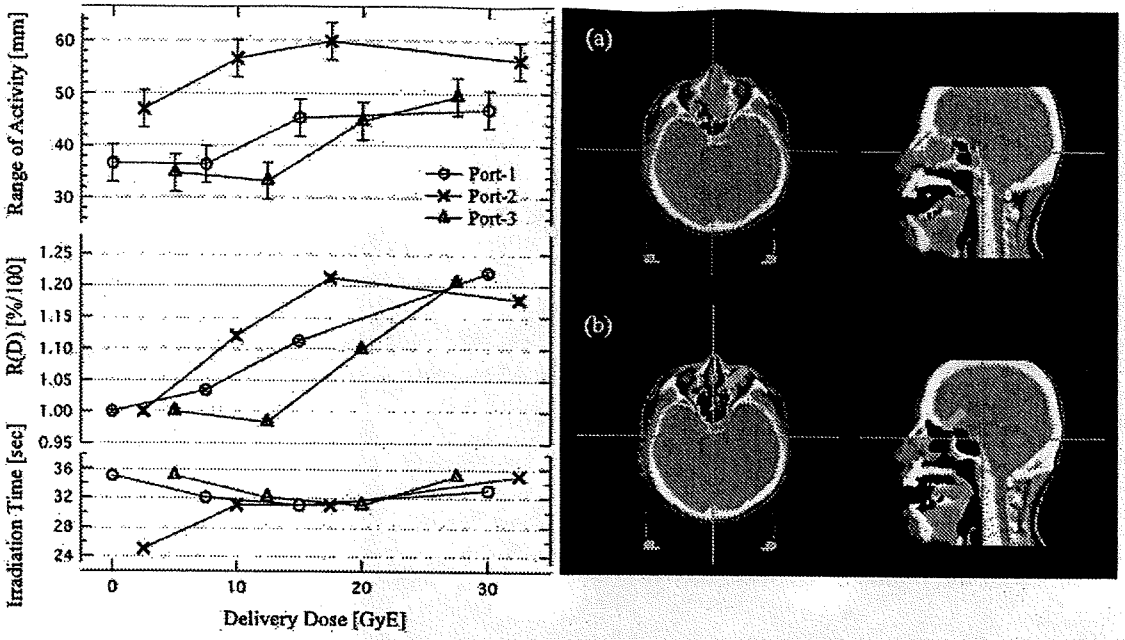

Fig. 6. Changes in the values of the activity range and proton beam irradiation time per fraction dose at each irradiation field of Port-1, Port-2, and Port-3. Axial and sagittal CT images of the head and neck before treatment (a) and after delivery doses of 35 GyE (b).

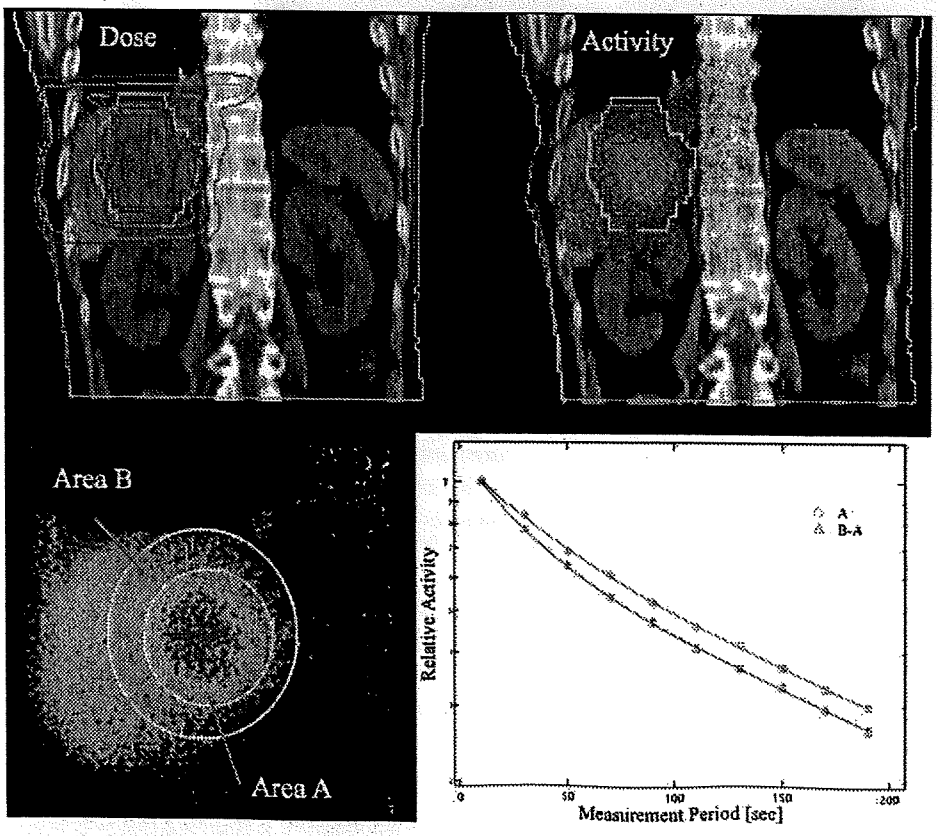

Fig. 7. The calculated dose distribution and the measured activity distribution on a CT image after the first treatment with a 3.8-GyE delivery dose, and the number of detection counts per 20 seconds of the activity in the region of interest (ROI) of areas A and B in the liver.

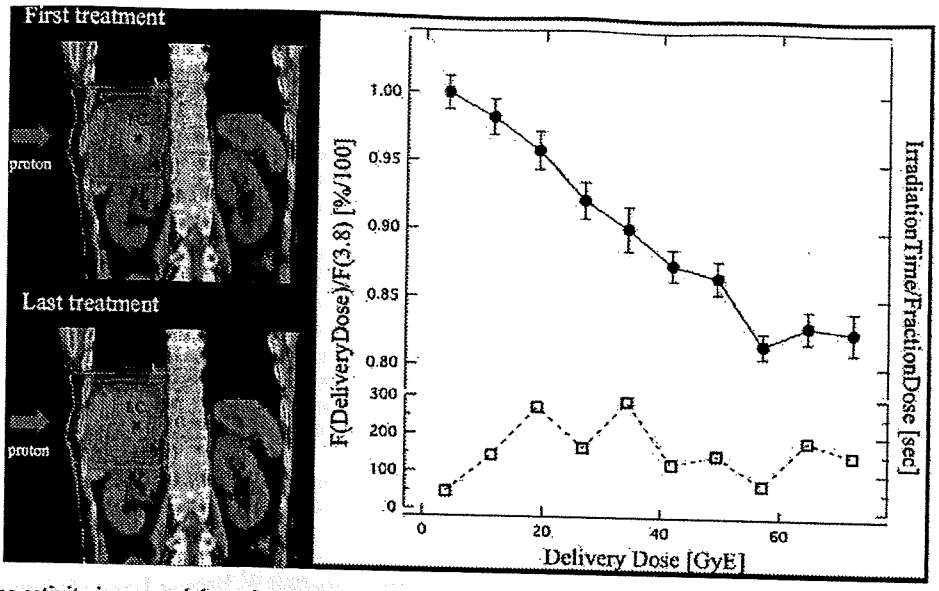

Fig. 8. The activity image and the ratio of the detection number to the measured activity calculated according to Equation (2) in the necrotic region of the liver tumor, and proton beam irradiation time per fractional dose.

the BOLPs-RGp and ^{11}C for measurements with the beam OFF-LINE PET system. As a tumor is equivalent to soft tissue, the measurement of the many ^{15}O nuclei generated in a tumor by proton irradiation is very important for the observation and evaluation of the changing form and the delivery dose response of the tumor. ^{12}C is present and ^{11}C is generated in the adipose tissue. Therefore, high activity is indicated in the region under the skin when using the beam OFF-LINE PET system. Furthermore, the BOLPs-RGp has the advantage of taking measurements with the patient in same position during proton irradiation. However, the CT image for the patient positioning can not be acquired at the same time as the activity measurement when using the BOLPs-RGp. This problem can be solved by the technological introduction of a CBCT.

At present, the length of activity measurement with the BOLPs-RGp after proton beam irradiation is 200 s; but, it may be possible that the measurement time can be shortened to less than 200 s as a result of this research. However, the measurement time must be determined with consideration to the detection efficiency by the delivery dose of each treatment site, the distance between the detector heads, and the activity measurement synchronized with the organ motion caused by respiration in the case of the liver and lungs.

The BOLPs-RGp has been used in the daily proton treatment of 48 patients. The monitoring of the accuracy of the proton beam irradiation was performed by comparing and verifying the daily activity images with reference activity images obtained at the start of the proton treatment. Specially, optimized proton treatment was performed by quickly replanning treatment in three clinical cases involving head-and-neck tumors, because different activity distribution were observed in the two images during the treatment period. The decrease of the activity in the region of necrotic cells in the liver tumor found during the histopathological examination was linked to an increase in the delivery dose. It is suggested that the increase in the washout effect in the necrotic region is caused by a decrease in the number of necrotic cells in the liver because of increased blood flow caused by the higher proton delivery dose. This effect may indicate a need to adapt the treatment to the dose response of the tumors in individual patients as well as the observation of the functional metabolism of organs.

The quality of the activity image is reduced by the large organ motion of the liver and the lungs. In cases of the prostate, the verification of changes in the activity distribution against the condition of the bladder and the position of the head of the femur will be reported in future. Moreover, a study concerning the experimental determination of cross sections of the target nuclear fragment reaction has been completed, and a simulation system that includes our cross-section data for calculating activity distribution in a patient's body with a high accuracy has been constructed using a cluster computer system. Many results of the research of the simulation have been already reported by the study group of Parodi *et al.* (12, 14). Finally, the ideal DGPT will be achieved through these developments and the research.

CONCLUSIONS

A BOLPs-RGp was constructed in our proton treatment room. The BOLPs-RGp has been used in many clinical cases. Report of the clinical use with beam ON-LINE PET or in-beam PET in the proton therapy has been never done before. The daily activity images obtained indicated the proton irradiation volume of the treatment administered to patients. Information about the positron-emitting nuclei provided by the BOLPs-RGp will be important for improving proton treatment accuracy in the future. DGPT (10) will thereby be achieved via daily proton treatment using the BOLPs-RGp.

REFERENCES

1. Oelfke U, Lam G, Atkins M. Proton dose monitoring with PET: Quantitative studies in Lucite. *Phys Med Biol* 1996;41: 177–196.
2. Litzenberg DW, Roberts DA, Lee MY, *et al.* On-line monitoring of radiotherapy beams: Experimental results with proton beams. *Med Phys* 1999;26:992–1006.
3. Parodi K, Enghardt W. Potential application of PET in quality assurance of proton therapy. *Phys Med Biol* 2000;45:N151–N156.
4. Nishio T, Ogino T, Shimbo M, *et al.* Distributions of b^+ decayed nucleus produced from the target fragment reaction in $(CH_2)n$ and patient liver targets by using a proton beam for therapy. *Abstr XXXIV PTCOG Mtg Boston* 2001;15–16.
5. Parodi K, Enghardt W, Haberer T. In-beam PET measurements of β^+ radioactivity induced by proton beams. *Phys Med Biol* 2002;47:21–36.
6. Hishikawa Y, Kagawa K, Murakami M, *et al.* Usefulness of positron-emission tomographic images after proton therapy. *Int J Radiat Oncol Biol Phys* 2002;53:1388–1391.
7. Enghardt W, Parodi K, Crespo P, *et al.* Dose quantification from in-beam positron emission tomography. *Radiother Oncol Suppl 2* 2004;73:S96–S98.
8. Nishio T, Sato T, Kitamura H, *et al.* Distributions of β^+ decayed nuclei generated in the CH_2 and H_2O targets by the target nuclear fragment reaction using therapeutic MONO and SOBP proton beam. *Med Phys* 2005;32:1070–1082.
9. Parodi K, Ponisch F, Enghardt W. Experimental study on the feasibility of in-beam PET for accurate monitoring of proton therapy. *IEEE Trans Nucl Sci* 2005;52:778–786.
10. Nishio T, Ogino T, Nomura K, *et al.* Dose-volume delivery guided proton therapy using beam ON-LINE PET system. *Med Phys* 2006;33:4190–4197.
11. Parodi K, Paganetti H, Cascio E, *et al.* PET/CT imaging for treatment verification after proton therapy: A study with plastic phantoms and metallic implants. *Med Phys* 2007;34: 419–435.
12. Parodi K, Paganetti H, Shih HA, *et al.* Patient study of in vivo verification of beam delivery and range, using positron emission tomography and computed tomography imaging after proton therapy. *Int J Radiat Oncol Biol Phys* 2007;68:920–934.
13. Nishio T, Miyatake A, Inoue K, *et al.* Experimental verification of proton beam monitoring in a human body by use of activity image of positron-emitting nuclei generated by nuclear fragmentation reaction. *Radiol Phys Technol* 2008;1: 44–54.
14. Parodi K, Ferrari A, Sommerer F, *et al.* Clinical CT-based calculations of dose and positron emitter distributions in proton therapy using the FLUKA Monte Carlo code. *Phys Med Biol* 2007;52:3369–3387.
15. Pawelke J, Enghardt W, Haberer T, *et al.* In-beam PET imaging for the control of heavy-ion tumour therapy. *IEEE Trans Nucl Sci* 1997;44:1492–1498.
16. Parodi K, Crespo P, Eickhoff H, *et al.* Random coincidences during in-beam PET measurements at microbunched therapeutic ion beams. *Nucl Instrum Meth A* 2005;545:446–458.
17. Uchida H, Okamoto T, Ohmura T, *et al.* A compact planar positron imaging system. *Nucl Instr Meth* 2004;A516:564–574.

Radiol Phys Technol
DOI 10.1007/s12194-010-0084-z

Evaluation of the usefulness of a MOSFET detector in an anthropomorphic phantom for 6-MV photon beam

Ryosuke Kohno · Eriko Hirano · Satoshi Kitou · Tomonori Goka · Kana Matsubara · Satoru Kameoka · Taeko Matsuura · Takaki Ariji · Teiji Nishio · Mitsuhiko Kawashima · Takashi Ogino

Received: 23 July 2009 / Revised: 7 January 2010 / Accepted: 8 January 2010

Abstract In order to evaluate the usefulness of a metal oxide-silicon field-effect transistor (MOSFET) detector as a in vivo dosimeter, we performed in vivo dosimetry using the MOSFET detector with an anthropomorphic phantom. We used the RANDO phantom as an anthropomorphic phantom, and dose measurements were carried out in the abdominal, thoracic, and head and neck regions for simple square field sizes of 10 × 10, 5 × 5, and 3 × 3 cm^2 with a 6-MV photon beam. The dose measured by the MOSFET detector was verified by the dose calculations of the superposition (SP) algorithm in the XiO radiotherapy treatment-planning system. In most cases, the measured doses agreed with the results of the SP algorithm within ±3%. Our results demonstrated the utility of the MOSFET detector for in vivo dosimetry even in the presence of clinical tissue inhomogeneities.

Keywords MOSFET detector · In vivo dosimetry · Anthropomorphic phantom · Inhomogeneity · Superposition algorithm

R. Kohno (✉) · E. Hirano · S. Kitou · T. Goka · S. Kameoka · T. Matsuura · T. Ariji · T. Nishio · M. Kawashima · T. Ogino
National Cancer Center Hospital East, 6-5-1 Kashiwanoha, Kashiwa, Chiba 277-8577, Japan
e-mail: rkohno@east.ncc.go.jp

R. Kohno
National Cancer Center Research Institute, 5-1-1 Tsukiji, Chuo-ku, Tokyo 104-0045, Japan

K. Matsubara
Graduate School of Human Health Sciences, Tokyo Metropolitan University, 7-2-10 Higashiogu, Arakawa-ku, Tokyo 116-8551, Japan

T. Matsuura
Foundation for Promotion of Cancer Research, 5-1-1 Tsukiji, Chuo-ku, Tokyo 104-0045, Japan

T. Nishio
Graduate School of Medicine, University of Tokyo, 7-3-1 Hongo, Bunkyo-ku, Tokyo 113-8655, Japan

Published online: 04 February 2010

1 Introduction

For implementation of radiation therapy with high-energy photon beams in the clinics, comprehensive dose verifications are essential. Generally, dose verifications on phantoms are recommended and carried out for each irradiation condition [1–4]. However, this does not mean that these verifications assure a perfect actual radiation dose to the patients. On the other hand, in vivo dosimetry can be used to identify major deviations in the delivery of treatment. Thus, we regard in vivo dosimetry during patient treatment as the ultimate dose verification for patient quality assurance (QA). Here, in order to carry out in vivo dosimetry, the detector must be very small, and easy to localize. To achieve this goal, we used metal oxide-silicon field-effect transistor (MOSFET) detectors (Best Medical Canada, Ottawa, Canada).

The MOSFET detector has a very small sensitive volume, which is a 0.2 mm × 0.2 mm, 0.5-μm-thick layer of insulating of silicon dioxide. The detector which we used is a dual-MOSFET detector consisting of two identical MOSFETs fabricated on the same silicon chip and operating at two different gate bias voltages, allowing temperature compensation of the detector response [5]. The MOSFET detector has been widely used for measuring radiation doses [6–11], and the accuracy, reliability, and usefulness of the MOSFET detector in clinical applications such as pinpoint absolute dosimetry has been reported [12].

An accurate estimate of the radiation dose is important for verifying that the expected dose of radiation has been delivered to the patient. Chuang et al. used a MOSFET detector in intensity-modulated radiation therapy (IMRT) dosimetric verification for routine IMRT phantoms, a solid water slab phantom, and a cylindrical PMMA phantom [7]. These dose verifications were performed on homogeneous materials. Carrasco et al. [13] measured percentage depth doses in inhomogeneous-layer phantoms containing water- and bone-equivalent materials using a MOSFET detector. The MOSFET detector was found suitable for dose measurement inside bone-equivalent materials. On the other hand, MOSFET detectors have previously been employed in surface dose measurements during in vivo dosimetry [8, 12, 14]. However, these measurements were not performed under the variable conditions created by inhomogeneous specimens containing water-, lung-, and bone-equivalent materials.

Here, we evaluated dose measurements using the MOSFET detector in inhomogeneous regular slab phantoms, as shown in "Appendix". The dose verification results for the superposition (SP) algorithm with use of the MOSFET detectors were similar to Kohno's results with use of the Farmer ionization chamber [15]. In general, the degree of accuracy in the dose measurement with MOSFET detectors is not as high as that with ionization chambers. However, we demonstrated that the MOSFET detector can measure doses with sufficient accuracy for various tissue-equivalent phantoms, various regular geometries, and various field sizes. From a different point of view, we can also say that it is important to measure dose independently using detectors with different characteristics, in order to evaluate the results of dose measurements in difficult irradiation conditions such as the presence of inhomogeneities.

On the other hand, the human body does not have a simple geometry such as the above regular slabs, and it forms complex inhomogeneities with bone, soft tissue, various materials, and various shapes. Therefore, it may not be certain that the results of dose verifications for slab-based phantoms can be extrapolated to actual clinical cases. In this paper, to evaluate the usefulness of the MOSFET detector as an in vivo dosimeter under more realistic conditions, we performed in vivo dosimetry using an anthropomorphic phantom.

2 Materials and methods

2.1 Experimental apparatus

Experiments were carried out with a Siemens ONCOR linear accelerator (Siemens Medical Solutions USA, Concord, CA) with a dual-focus, multi-leaf collimator. The specified uncertainty of the leaf positions was ± 1 mm. For dose measurements, we used TN-502RD MOSFET detectors and the mobileMOSFET reader, set at the standard bias sensitivity. The MOSFET and a calibrated 0.6 cc Farmer ionization chamber type 30013 (PTW, Freiburg, Germany) were placed in a dose calibration phantom made of PMMA. Tough Water phantoms manufactured by Kyoto Kagaku Co., Ltd (Kyoto, Japan) were stacked on the dose calibration phantom. With a 6-MV photon beam at a dose rate of 300 MU/min, a dose of 100 MU was delivered at 100 cm source-to-axis distance (SAD), at a depth of 10 cm within a field of 10×10 cm^2 for calibration of the MOSFET response.

Measurements were carried out for simple square field sizes of 10×10, 5×5, and 3×3 cm^2 with a 6-MV photon beam. All measurement points were set in the center of an exposed square area. We used a beam angle of 0° for all of the experiments, thus avoiding uncertainties ($\sim 2\%$) of angular dependence [7, 11] of the MOSFET detector in the dose measurements, and unnecessary complexities in the SP dose calculations. We estimated the reproducibility as $\pm 1.5\%$ (1 standard deviation) for five consecutive irradiations of 100 MU each.

2.2 Anthropomorphic phantom

The RANDO anthropomorphic phantom (The Phantom Laboratory, Salem, CA) [16] provides a detailed mapping of the dose distribution that is essential for evaluating radiotherapy treatment plans. RANDO phantoms are constructed with a natural human skeleton cast inside a material that is radiologically equivalent to soft tissue. The RANDO lungs are molded to fit the contours of the natural human rib cage. The properties of the RANDO materials are listed in Table 1. The ρ_{nominal} value is the nominal electron density relative to water for tissue-equivalent materials. Physical densities and effective atomic numbers of the tissue-equivalent materials are also shown in Table 1. The MOSFET detectors were placed within cavities in the phantom.

First, the detector positions were selected in the abdominal region. As shown in Fig. 1a and b, the abdominal region in the phantom is homogeneous. The measurement point is indicated by a cross mark, and the measurement depths for Fig. 1a and b were 6 and 9.5 cm, respectively.

Next, the dose measurement points for the chest region are illustrated in Fig. 2a–c. Figure 2a depicts a region of the mediastinum, which is a soft tissue. This measurement point is at an interface of the mediastinum and lung, with the beam central axis in the interface. On the other hand, Fig. 2b and c is in the lung region, and thus we were able to

Table 1 Electron densities relative to water obtained by CT number conversion (ρ_{meas}), effective atomic number, and physical densities of the tissue-equivalent materials in the RANDO phantom used in this study

Phantom	Soft tissue	Lung
$\rho_{nominal}$	0.979	0.311
ρ_{meas}	1.014 ± 0.003	0.231 ± 0.015
Effective atomic number	7.60	7.11
Physical density (g/cm^3)	0.997	0.352

$\rho_{nominal}$ nominal electron density relative to water

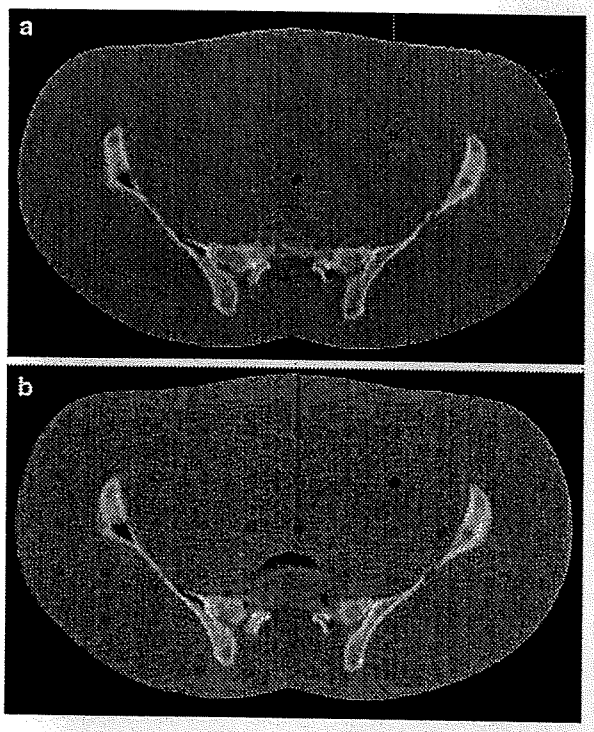

Fig. 1 The homogeneous abdominal region of the anthropomorphic phantom. The measurement point is indicated by a *cross mark*, and the measurement depths for **a** and **b** were 6 and 9.5 cm, respectively. Measurements were carried out for simple square field sizes of 10 × 10, 5 × 5, and 3 × 3 cm^2 and a beam angle of 0° with a 6-MV photon beam. All measured points were set in the center of an exposed square area

evaluate the dose for low-density material. The measurement depths for Fig. 2b and c were 4.5 and 7.5 cm, respectively.

Figure 3a, b, and c illustrates measurement locations in the head and neck region. In Fig. 3a, the dosimeter is located at the center of the posterior arch of the first cervical vertebra in the RANDO phantom. The dose here was formed by the photon beam passing through the jaw, consisting of cortical bone, and the oral cavity, consisting of air. Figure 3b is the location posterior to the sella in the RANDO phantom, which corresponds to the surface of the brainstem. This region also consists of bone, cavities, and soft tissue, and forms complex inhomogeneities. Because of the presence of many critical structures, it is important to deliver accurate doses in this region. Figure 3c is a location posterolateral to the posterior arch of the first cervical vertebra.

2.3 Dose calculation and data analysis

The XiO 4.33.02 radiotherapy planning (RTP) system for dose calculations was used in this study. Doses were calculated using SP algorithm [17] with inhomogeneity correction. Here, the Monte Carlo (MC) method as a dose calculation algorithm is a powerful tool for analytic calculations and for verification of results obtained in difficult measurements situations. However, because the MC has considerable difficulties and uncertainties in reconstructive techniques based on measured depth dose distributions for clinical photon beams [18], we did not use it in this study. On the other hand, the SP has already been verified for various irradiation conditions by many authors [15, 17–21, "Appendix"] and has been widely adopted in clinical use. Therefore, using the SP as a dose calculation algorithm is reasonable for comparing the calculation dose with the MOSFET dose in this study. Three-dimensional dose distributions were calculated with 0.2 cm resolution.

Phantom information was obtained from computed tomography (CT) images. The CT images of all phantoms were acquired with an Asteion (Toshiba Medical Systems Corp., Tokyo, Japan) CT scanner at a 2.5 mm slice thickness and 2.5 mm slice separation. The electron density of each tissue, ρ_{meas}, is obtained by CT number conversion, and we used this value obtained by CT scan in our dose calculations. Here, the ρ_{meas} of the lung material in Table 1 was somewhat smaller than the $\rho_{nominal}$. We assume that the lung material of the RANDO phantom changed over time. This may have led to overestimates in the dose calculations.

Dosimetric magnitudes were analyzed in terms of absolute doses. D_{calc} is the calculated dose at a measurement point in the phantom, and D_{meas} is the measured dose at the same point. The dose measured at each point was compared to the calculated dose, and the discrepancy at the measurement point, $\delta(\%)$, was evaluated as a percentage of the measured dose:

$$\delta(\%) = \frac{D_{calc} - D_{meas}}{D_{meas}} \times 100.$$

The error bars in each figure represent the reproducibility of the MOSFET dose.

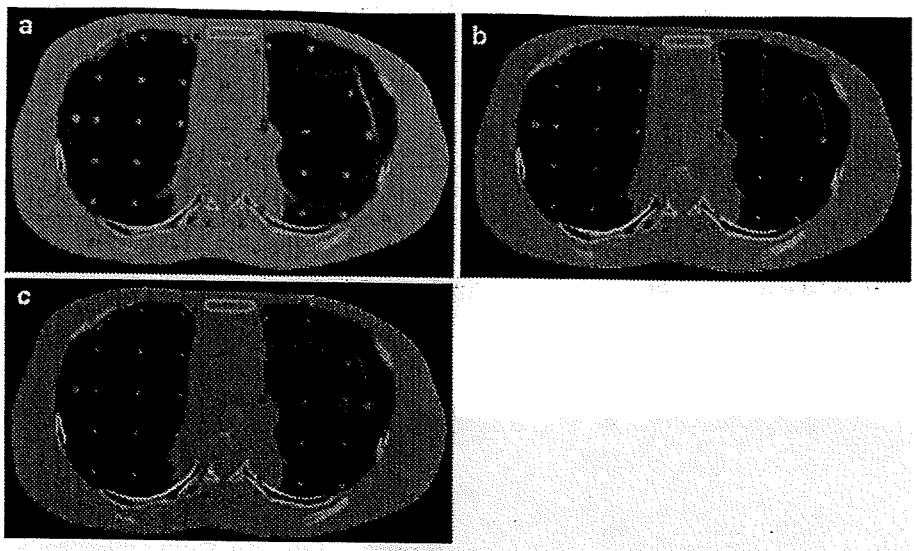

Fig. 2 The chest region of the anthropomorphic phantom. The *cross marks* represent the measurement point. **a** A region of the mediastinum. **b** and **c** The lung region. The measurement depths for **b** and **c** were 4.5 and 7.5 cm, respectively. Measurements were carried out for simple square field sizes of 10×10, 5×5, and 3×3 cm^2 and a beam angle of 0° with a 6-MV photon beam. All measured points were set in the center of an exposed square area

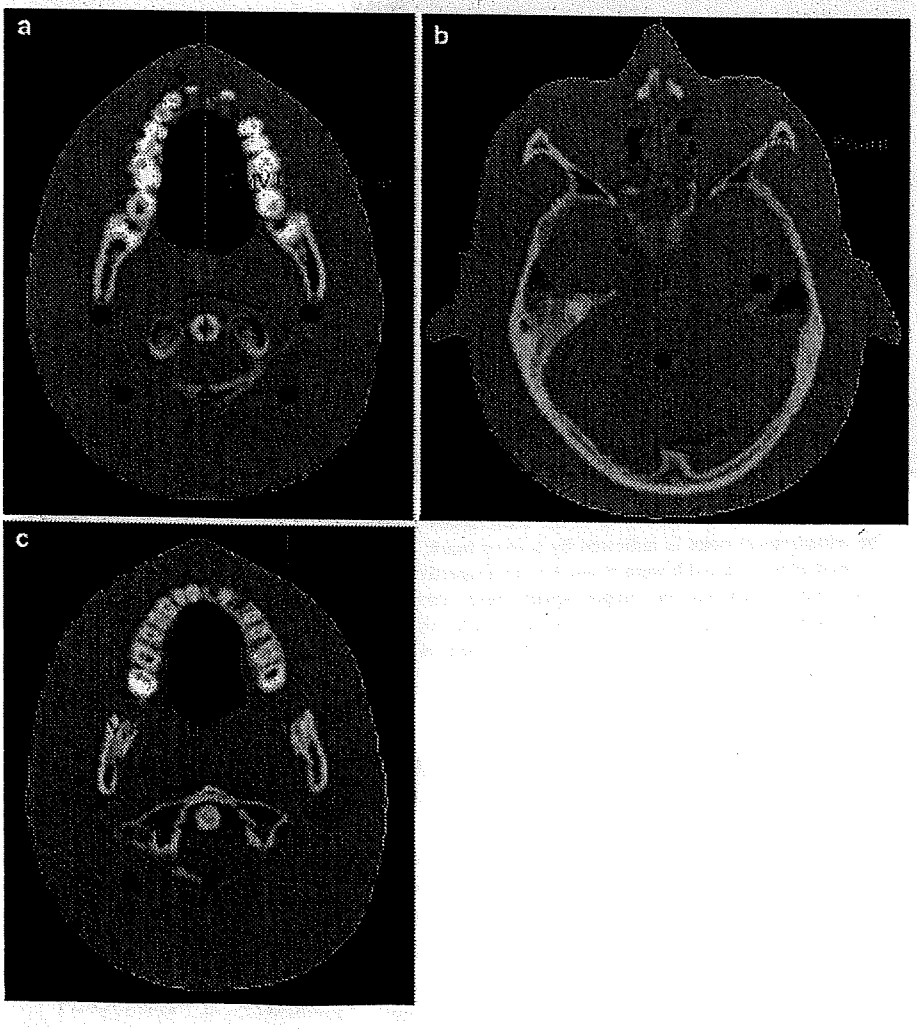

Fig. 3 The head and neck region of the anthropomorphic phantom. The *cross marks* represent the measurement point. **a** The dosimeter is located at the center of the posterior arch of the first cervical vertebra in the RANDO phantom. **b** The location posterior to the sella in the RANDO phantom. **c** A location posterolateral to the posterior arch of the first cervical vertebra. Measurements were carried out for simple square field sizes of 10×10, 5×5, and 3×3 cm^2 and a beam angle of 0° with a 6-MV photon beam. All measured points were set in the center of an exposed square area

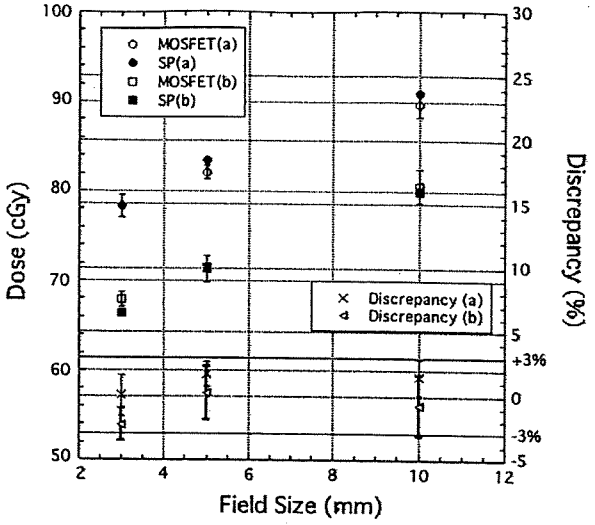

Fig. 4 Comparisons between the doses measured with the MOSFET detector and doses calculated by use of the SP algorithm for the homogeneous abdominal region of Fig. 1. The measurement depths for **a** and **b** were 6 and 9.5 cm, respectively. This figure also includes the discrepancy (%) between doses measured with the MOSFET detector and doses calculated with the SP algorithm

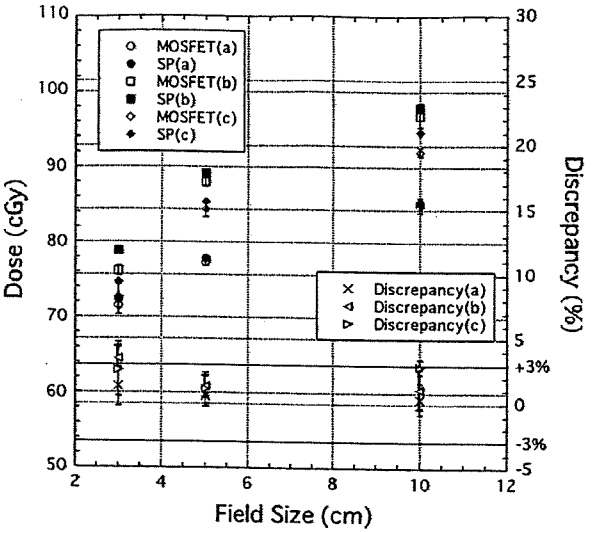

Fig. 5 Comparisons between the doses measured with the MOSFET detector and doses calculated by use of the SP algorithm for the chest region of Fig. 2. Evaluation point (Fig. 2a) is a region of the mediastinum, and **b** and **c** are in the lung region. The measurement depths for Figs **2b** and **c** were 4.5 and 7.5 cm, respectively. This figure also includes the discrepancy (%) between doses measured with the MOSFET detector and doses calculated with the SP algorithm

3 Results and discussion

Figure 4 contains comparisons between doses measured with the MOSFET detector and doses calculated by the SP method for soft tissue for Fig. 1a and b, respectively. This figure also includes the discrepancy (%) between doses measured with the MOSFET detector and doses calculated with the SP algorithm. The measured doses agreed with the results of the SP algorithm within ±3%.

Comparisons between the measurements and calculations for the chest region (Fig. 2a–c) are displayed in Fig. 5. We observed that the SP overestimates the dose particularly in the lung region (Fig. 2b, c) compared with the measurements. We can explain this by an underestimation by use of the relative electron density for lung material, as shown in Table 1. Then, the difference of the doses between MOSFET and SP at a field size of 3 cm is larger than those at 5 and 10 cm. Because the leaf position uncertainty of ±1 mm contributes approximately 0.5% to the dose uncertainty for the 3 × 3 cm^2 field size, it may be one of the causes of the larger difference.

Figure 6 depicts comparisons between doses measured with the MOSFET detector and doses calculated with the SP algorithm for the head and neck measurements mapped in Fig 3a–c. Here, Kohno et al. [15] reported that a definite deterioration in the dose prediction accuracy occurred when they used the SP algorithm in bone material for a field size of 3 × 3 cm^2. Moreover, Fig. 8c also supported the deterioration. Therefore, the SP algorithm would display significant differences in Fig. 3a due to the inadequate energy deposition kernel model for bone material [19]. However, even in this complex inhomogeneous region, the measured doses agreed with the results of the SP algorithm within ±3%. We concluded that the actual body does not include large and thick bones such as this in Fig. 7c, which results in a large deterioration of the dose prediction due to the incomplete energy deposition kernel model in the photon dose calculation.

Thus, dose measurements by use of the MOSFET detector were compared with calculations by the SP algorithm for various irradiation conditions. The small size, immediate read-out, and fast response of the MOSFET detector make it particularly useful for dose measurements for therapeutic MV photon beams. The results of our dosimetric measurements demonstrate the utility of the MOSFET detector for clinical dosimetry in radiotherapy. Our dose measurements were performed at a beam angle of 0°. Given the variety of beam angles used in actual radiotherapy, the ±2% angular dependence of the MOSFET detector must be considered [7, 11]. The angular dependence may lead to a decrease in accuracy at some angles, which, in turn, may affect the clinical utility of this detector.

4 Conclusion

We evaluated in vivo dosimetry with a MOSFET detector for an anthropomorphic phantom. Dose measurements

were carried out in the abdominal, thoracic, and head and neck regions for simple square field sizes of 10 × 10, 5 × 5, and 3 × 3 cm^2 with a 6-MV photon beam. The measured dose agreed with the results obtained with the SP algorithm to within ±3%. The MOSFET detector as an in vivo dosimeter was useful for pinpoint absolute dosimetry even in the presence of clinical tissue inhomogeneities.

Acknowledgments The authors would like to express their gratitude to A. Hallil of Best Medical Canada Ltd. for his technical advice and support. The authors also thank Yu Furuhata, AcroBio Corporation, for his support.

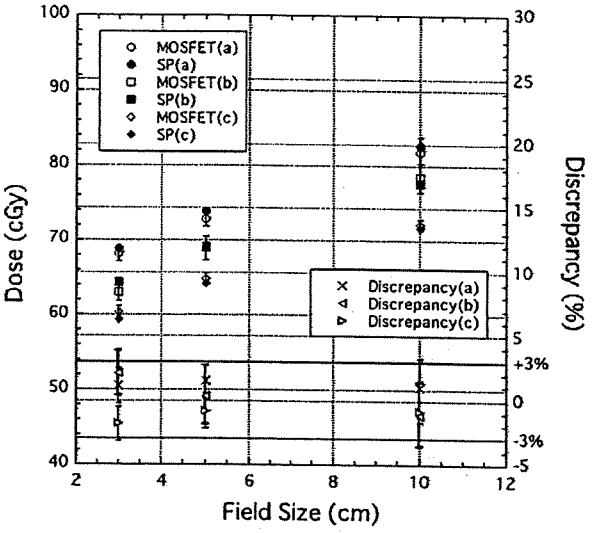

Fig. 6 Comparisons between the doses measured with the MOSFET detector and doses calculated by use of the SP algorithm for the head and neck region of Fig. 3. The dosimeter of Fig. 3 is located at the center of the posterior arch of the first cervical vertebra. Figure 3b and c are the location posterior to the sella and the location of posterolateral to the posterior arch of the first cervical vertebra. This figure also includes the discrepancy (%) between doses measured with the MOSFET detector and doses calculated with the SP algorithm

Appendix

Evaluation of dose measurements by use of a MOSFET detector in inhomogeneous slab phantoms for 6 MV photon beam (Figs. 7, 8, 9, and 10)

We summarize the dose evaluations by use of the MOSFET detector in multi-layer and laterally inhomogeneous phantoms, the geometries of which were the same as those in the study of Kohno et al. [15]. Doses measured by the MOSFET detector were compared to these point doses calculated by the SP algorithm with inhomogeneity correction in the same RTP system. Experiments were carried out with the same beam conditions, 6 MV, dose rate of 300 MU/min, beam angle of 0°, and square field sizes of 10 × 10, 5 × 5, and 3 × 3 cm^2. A dose of 100 MU was delivered 5 times at 100 cm SAD. In these measurements, a tough water phantom (TW), tough lung phantom (TL), tough bone BE-H phantom (TB) (Kyoto Kagaku Co., Ltd, Kyoto, Japan), and a PMMA phantom were used (Table 2).

Figure 7 illustrates the layout of the TW and PMMA phantoms for the TW, TL, and TB thicknesses of 9 cm (a), 9 cm (b), and 4 cm (c). These phantom geometries can be used for checking the dose levels beyond a lung or bone

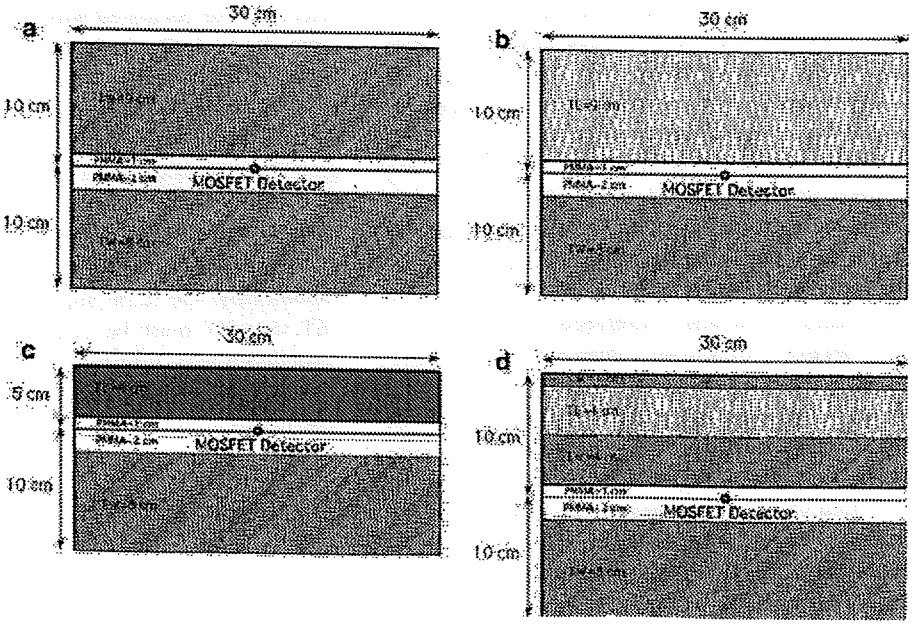

Fig. 7 Multi-layer phantom geometries of the **a** TW and PMMA phantoms for TW thicknesses of 9 cm, **b** TL phantom with a thickness of 9 cm, **c** TB phantom with a thickness of 4 cm, and **d** TW + TL + TW phantom. Measurements were carried out for simple square field sizes of 10 × 10, 5 × 5, and 3 × 3 cm^2 and a beam angle of 0° with a 6-MV photon beam

structure. Figure 7d demonstrates the typical geometry of a thoracic wall-lung-thoracic wall interface.

Figure 8 shows a comparison between doses measured with the MOSFET detector and doses calculated with the SP algorithm for the phantoms of Fig 7. This figure also includes a discrepancy (%) of doses measured with the MOSFET detector and doses calculated with the SP algorithm. The measured results for the (a) TW 9 cm and the (b) TL 9 cm phantom were within 1.5% of the corresponding calculation. For the (c) TB 4 cm phantom, the measured results were within 2.5% of the calculated values for field sizes of 10 × 10 and 5 × 5 cm^2. However, for a field size of 3 × 3 cm^2, the dose measurement underestimated the calculated dose by 5.5%. Although the difference increased with decreasing field size, the leaf position uncertainty of ±1 mm may have contributed approximately 1% to the dose uncertainty for the 3 × 3 cm^2 field size. However, this cannot account for the entire uncertainty. This discrepancy is comparable to that reported by Kohno et al. [15]; therefore, we estimated that this is because the bone material is equivalent to water (i.e., has the same atomic properties) in the dose calculation [19]. In fact, electrons released in materials with higher atomic numbers are scattered at wider angles compared to electrons generated in water. For the (d) TW + TL + TW phantom, the results at a point beyond a typical thoracic wall-lung-thoracic wall interface from the MOSFET measurements agreed with the SP calculations to around 3% for each field size.

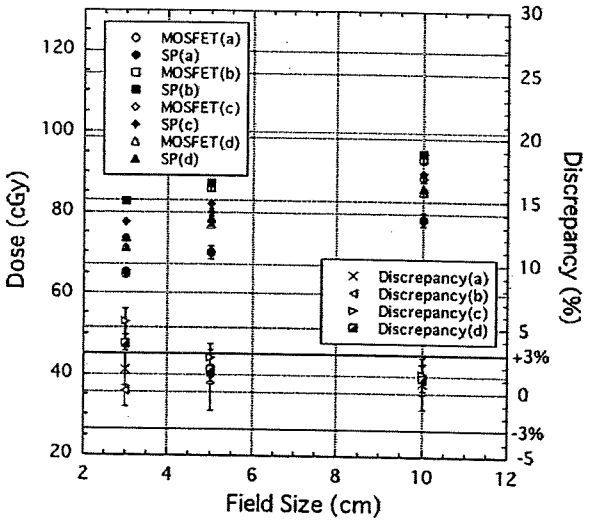

Fig. 8 Comparisons between the measurement dose from a MOSFET detector and doses calculated using the SP algorithms for the multilayer phantom geometries of the Fig 1a TW 9 cm, b TL 9 cm, c TB 4 cm, and d TW + TL + TW phantom. This figure also includes discrepancy (%) of doses measured with the MOSFET detector and doses calculated with the SP algorithm

Figure 9a–c depicts the three laterally inhomogeneous phantom geometries. Figure 9a and b model a mediastinum/lung interface with the beam central axis in the interface. Figure 9c represents a TB/TL interface. For these configurations, because we expected the phantom setups to have a considerable effect on the dose at the measurement point, each dose measurement was performed independently twice.

Figure 10 depicts the measured and calculated absolute doses for each laterally inhomogeneous phantom, as well as the dose profile calculated by the SP algorithm, because the measurement point has a gradient dose distribution in the lateral direction. From this dose profile, we can estimate the effect of the phantom setup uncertainty.

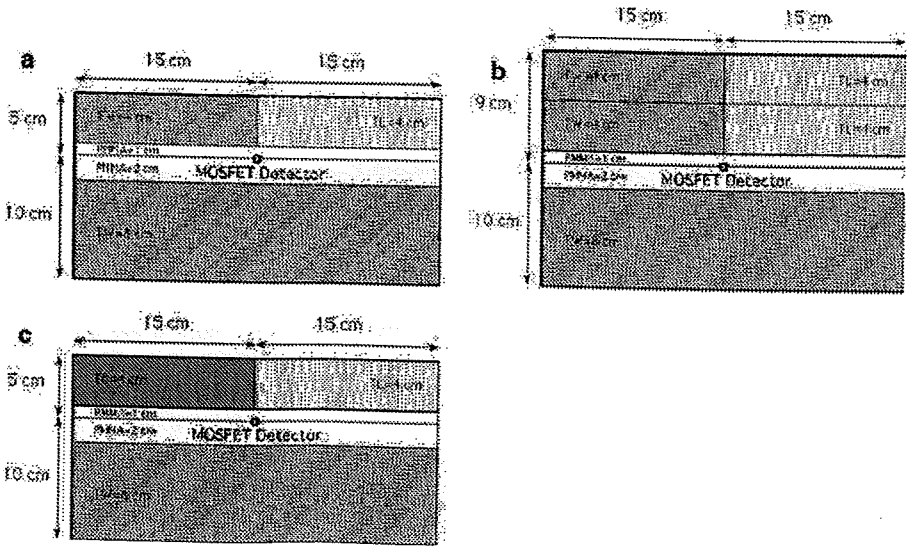

Fig. 9 Laterally inhomogeneous phantom geometries of the a TW/TL interface with the beam central axis in the interface, b TB/TL interface, and c larger TW/TL interface. Measurements were carried out for simple square field sizes of 10 × 10, 5 × 5, and 3 × 3 cm^2 and a beam angle of 0° with a 6-MV photon beam

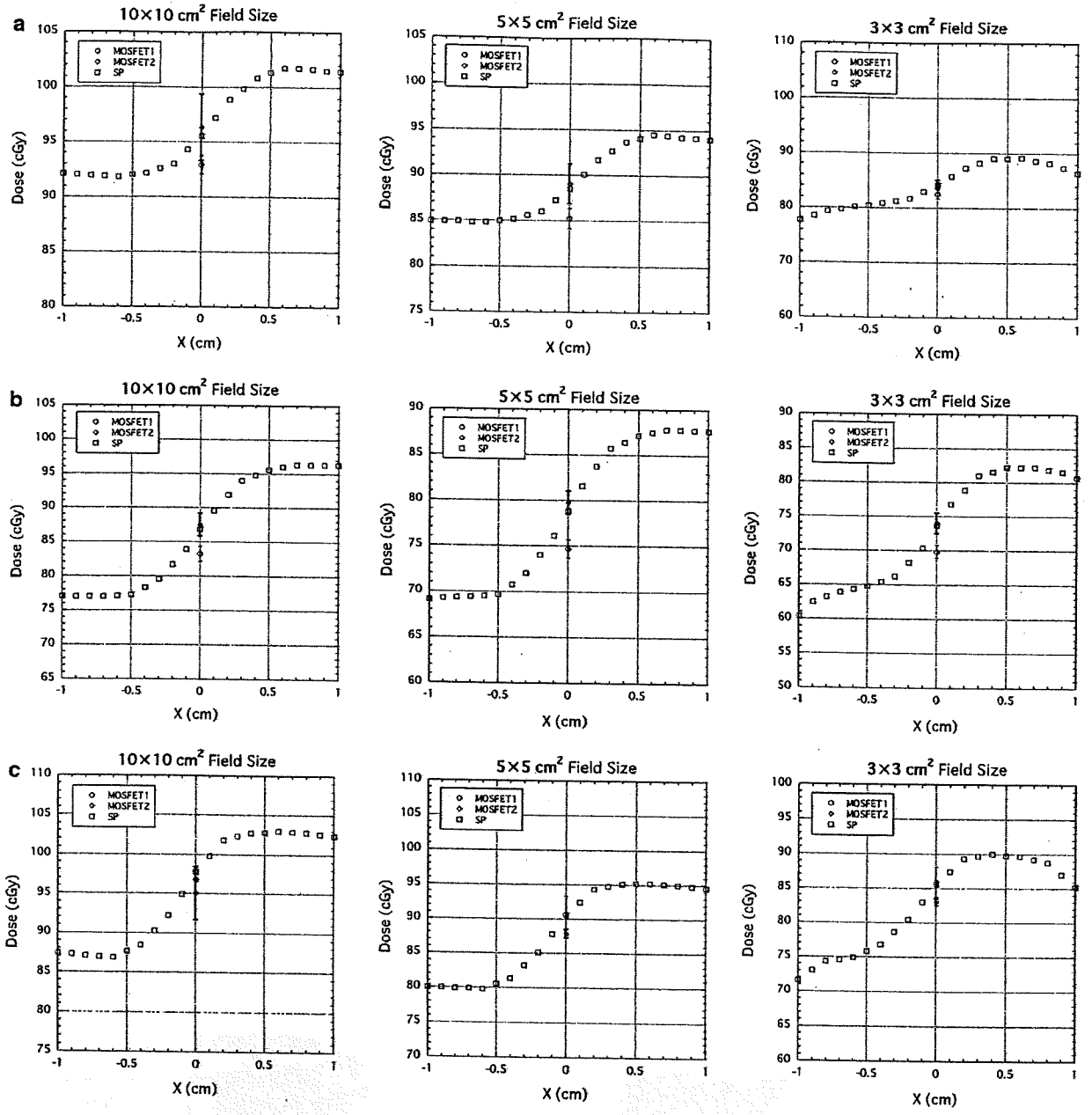

Fig. 10 Comparisons between the measurement dose from a MOSFET detector and doses calculated using the SP algorithm for the laterally inhomogeneous phantom geometries of the Fig 2a TW/TL interface, b TB/TL interface, and c larger TW/TL interface. This figure also includes the dose profile calculated by the SP algorithm

Figure 10a and b depicts the measured and calculated absolute doses at the TW/TL interface, and the measurement points had a gradient dose distribution of 1.5–5%/mm in the lateral direction. Most results agreed with the SP calculations within 3%. Although the maximum difference was +5.6% for a field size of 5 × 5 cm^2 in Fig. 10b, we could explain this large difference as the effect of the phantom setup uncertainty of ±1 mm. Thus, this highlights the difficulty in point dose measurement with a small radiation detector. The measured and calculated doses for the TB/TL interface are plotted in Fig. 10c. The results of the MOSFET measurement agreed with the SP calculations within 3%, in spite of the fact that the measurement point had a gradient dose distribution of 3%/mm in the lateral

Table 2 Electron densities relative to water obtained by CT number conversion (ρ_{meas}), effective atomic number, and physical densities of the tissue-equivalent materials used in this study

Phantom	Tough water	Tough lung	Tough bone	PMMA
$\rho_{nominal}$	0.990	0.313	1.416	1.148
ρ_{meas}	1.013 ± 0.006	0.320 ± 0.023	1.395 ± 0.003	1.137 ± 0.006
Effective atomic number	7.44	7.77	11.70	6.47
Physical density (g/cm^3)	1.017	0.320	1.500	1.190

$\rho_{nominal}$ nominal electron density relative to water

direction. The kernel model for bone material in the SP algorithm did not significantly affect the dose accuracy in this case.

Doses measured by the MOSFET detector in inhomogeneous regular slab phantoms were compared to those calculated by the SP algorithm in the XiO radiotherapy treatment-planning system. Except for the TB phantom at the small field size, the results of the MOSFET detector agreed with the calculated doses to within 3%. We reconfirmed and support the results of Kohno's study [15] with dose measurements with the MOSFET detector. The MOSFET detector was useful for pinpoint dosimetry even in inhomogeneous slab media.

References

1. Nishio T, Kohno R, Mori S, Mizuno H, Hanyu Y, Takahashi Y. Quality assurance of treatment planning systems for X-ray beams. Jpn J Med Phys. 2008;27(6).
2. IAEA Technical Reports Series No. 430. Comissioning and quality assurance of computerized planning systems for radiation treatment of cancer. Vienna: IAEA; 2005.
3. Fraass B, Doppke K, Hunt M, Kutcher G, Starkschall G, Stern R, et al. Quality assurance for clinical radiotherapy treatment planning. Med Phys. 1998;25:1773–829.
4. ESTRO Booklet No. 7. Quality assurance of treatment planning systems practical examples for non-IMRT photon beams. Brussels: ESTRO; 2004.
5. Soubra M, Cygler J, Mackay G. Evaluation of a dual bias dual metal oxide-silicon semiconductor field effect transistor detector as radiation dosimeter. Med Phys. 1994;21:567–72.
6. Ramaseshan R, Kohil KS, Zhang TJ, Lam T, Norlinger B, Hallil A, et al. Perfomance characteristics of a microMOSFET as an in vivo dosimeter in radiation therapy. Phys Med Biol. 2004; 49:4031–48.
7. Chuang CF, Verhey LJ, Xia P. Investigation of the use of MOSFET for clinical IMRT dosimetric verification. Med Phys. 2002;29:1109–15.
8. Ramaseshan R, Stephen R, Peter O. Clinical dosimetry using MOSFETs. Int J Radiat Oncol Biol Phys. 1997;37:959–64.
9. Kohno R, Nishio T, Miyagishi T, Hirano E, Hotta K, Kawashima M, et al. Experimental evaluation of a MOSFET dosimeter for proton dose measurements. Phys Med Biol. 2006;51:6077–86.
10. Gurp EJB, Minken AWH, Mijnheer BJ, Dehing-Oberye CJG, Lambin P. Clinical implementation of MOSFET detectors for dosimetry in electron beams. Radiother Oncol. 2006;80:288–95.
11. Kohno R, Hirano E, Nishio T, Miyagishi T, Goka T, Kawashima M, et al. Dosimetric evaluation of a MOSFET detector for clinical application in photon therapy. Radiol Phys Technol. 2008; 1:55–61.
12. Marcie S, Charpiot E, Bensadoun RJ, Ciais G, Herault J, Costa A, et al. In vivo measurements with MOSFET detectors in oropharynx and nasopharynx intensity-modulated radiation therapy. Int J Radiat Oncol Biol Phys. 2005;61:1603–6.
13. Carrasco P, Jornet N, Duch MA, Panettieri V, Weber L, Eudaldo T, et al. Comparison of dose calculation algorithms in slab phantoms with cortical bone equivalent heterogeneities. Med Phys. 2007;34:3323–33.
14. Cherpak A, Studinski RCN, Cygler JE. MOSFET detectors in quality assurance of tomotherapy treatments. Radiother Oncol. 2008;86:242–50.
15. Kohno R, Kitou S, Hirano E, Kameoka S, Goka T, Nishio T, et al. Dosimetric verification in inhomogeneous phantom geometries for the XiO radiotherapy treatment planning system with 6 MV photon beams. Radiol Phys Technol. 2009;2:87–96.
16. Kleck JH, Smathers JB, Holly FE, Myers LT. Anthropomorphic radiation therapy phantoms: a quantitative assessment of tissue substitutes. Med Phys. 1990;17:800–6.
17. Miften M, Wiesmeyer M, Monthfer S, Krippner K. Implementation of FFT convolution and multigrid superposition models in the FOCUS RTP system. Phys Med Biol. 2000;45:817–33.
18. AAPM report No. 85. Tissue inhomogeneity corrections for megavoltage photon beams. Madison: Medical Physics Publishing; 2004.
19. Miften M, Wiesmeyer M, Kapur A, Ma CM. Comparison of RTP dose distributions in heterogeneous phantoms with the BEAM Monte Carlo simulation system. J Appl Clin Med Phys. 2001; 67:21–31.
20. Garcia-Vicente F, Minambres A, Jerez I, Modolell I, Torres JJ. Experimental validation tests of fast Fourier transform convolution and multigrid superposition algorithms for dose calculation in low-density media. Radiother Oncol. 2003;67:239–49.
21. Fogliata A, Vanetti E, Albers D, Brink C, Clivio A, Knoos T. et al. On the dosimetric behaviour of photon dose calculation algorithms in the presence of simple geometric heterogeneities: comparison with Monte Carlo calculations. Phys Med Biol. 2007;52:1363–85.

Jpn. J. Med. Phys. Vol. 28 No. 4: 172–206 (2009)

Review

Research on Radiation Protection in the Application of New Technologies for Proton and Heavy Ion Radiotherapy

Hirohiko TUJII[1)], Takashi AKAGI[3)], Keiichi AKAHANE[1)], Yoshitomo UWAMINO[2)], Tatsuya ONO[4)], Tatsuaki KANAI[1)], Ryosuke KOHNO[8)], Takeji SAKAE[5)], Masakazu SHIMIZU[3)], Eriko URAKABE[11)], Takashi NAKAYAMA[6)], Takashi NAKAMURA[7)], Teiji NISHIO[8)], Kanae NISHIZAWA[1)]*, Kunihide NISHIZAWA[9)], Shigekazu FUKUDA[1)], Naruhiro MATSUFUJI[1)], Haruo YAMASHITA[11)] and Shunsuke YONAI[1)]

[1)] National Institute of Radiological Sciences (NIRS), [2)] RIKEN, [3)] Hyogo Ion Beam Medical Center (HIBMC), [4)] Wakasa Wan Energy Research Center (WERC), [5)] Tohoku University, [6)] Radiation Safety Technology Center (NUSTEC), [7)] Clinical Analysis Center, National Cancer Center Hospital East (NCCHE), [8)] Nagoya University, [9)] Gunma University Heavy Ion Medical Center, [10)] Proton Medical Research Center, University of Tsukuba (PMRC), [11)] Shizuoka Cancer Center (SCC)

Keywords: Charged Particle Radiotherapies, Dose for medical workers, Radioactivity concentrations of the air, Waste water concentrtion

Abstract

Particle radiotherapy using proton and heavy ion beams has shown improved clinical results and is a promising cancer therapy which is expected to gradually spread in Japan. There are, however, no special regulations for radiotherapy treatment facilities. They have been operated under the same safety regulations as for a research facility using a research accelerator.

Significantly high-energy radiation is necessary for particle radiotherapy compared with conventional radiation therapy. The treatment facility, therefore, should have a large accelerator, which is installed in a room with a thick shield wall. Data on radiation protection for such high energy medical facilities is fragmentary and insufficient.

In this study, we examined the necessity of other regulations for the safe operation of medical facilities for particle radiotherapy. First, we measured activation levels of the therapeutic devices and of patients. Next the safety level of the medical facility was evaluated from the viewpoint of radiation protection. We have confirmed the facilities can be safely operated by present regulations given in the Law Concerning Prevention from Radiation Hazards due to Radiation Isotopes, etc. or the Law for Health Protection and Medical Care.

Received: December 25, 2008; accepted January 7, 2009

* Radiological Protection Section, Research Center for Charged Particle Therapy, National Institute of Radiological Sciences, 4–9–1 Anagawa, Inage-ku, Chiba 263–8555, Japan.
E-mail: nisizawa@nirs.go.jp

Contents

1. Purpose ····· 174
2. Charged Particle Radiotherapy ····· 174
   1. Characteristics of charged particle radiotherapy
   2. Energies of charged particles for radiotherapy
3. Materials and Methods ····· 174
4. Results and Discussion ····· 175
   4.1. Trends in international regulations for proton and heavy ion radiotherapies
   4.2. Estimation of dose exposure to radiation workers from activated materials ····· 177
      4.2.1. Aim of the study
      4.2.2. Devices of interest
         4.2.2.1. Multi-leaf collimator
         4.2.2.2. Patient collimator
         4.2.2.3. Patient compensator (bolus)
         4.2.2.4. Tissue substitute
      4.2.3. Measuring instrument
      4.2.4. Experiments
         4.2.4.1. Multi-leaf collimator
         4.2.4.2. Patient collimator
         4.2.4.3. Patient compensator
         4.2.4.4. Tissue substitute
      4.2.5. Data analysis
      4.2.6. Estimation of exposure dose
         4.2.6.1. Estimation of exposure dose at a carbon ion radiotherapy facility (NIRS)
         4.2.6.2. Estimation of exposure dose at proton radiotherapy facilities
         4.2.6.3. Results and discussions on the exposed dose to radiation technologists
         4.2.6.4. Exposure of patient's family members and effects on the environment
   4.3. Radioactive concentrations of the treatment room air and exhaust from facilities ····· 183
      4.3.1 Air activation with particle radiotherapy
         4.3.1.1 Air activation by charged particles
         4.3.1.2. Air activation by secondary neutrons
      4.3.2. Waste water concentration at treatment facilities
   4.4. Measurement of neutron ambient dose equivalent in passive carbon ion and proton radiotherapies ····· 188
      4.4.1. Methods and materials
      4.4.2. Result
5. Conclusion ····· 191
References ····· 193
Appendix I. Measurements of radioactivity induced in charged particle radiotherapy ····· 194
II. Study organization ····· 206

1. Purpose

This study looked at problems in radiation protection for staff workers and for families of patients during radiotherapy using new technologies.

2. Charged Particle Radiotherapies

The term "heavy particle" is used in Japanese to describe ions with a mass number of the nucleus larger than 1. We call the charged particle radiotherapy which uses these accelerated "heavy particles" as "heavy particle therapy" in Japanese. For this English report, we use the expression "charged particle radiotherapy" for "heavy particle therapy" used in Japanese. In this text, we include radiotherapy using protons in "charged particle radiotherapy".

In 1946, Robert Wilson proposed a clinical application of high energy protons for radiotherapy. The first clinical applications of these protons were made at Lawrence Berkeley Laboratory (LBL) of the University of California. Later, helium ions were continuously applied for radiotherapy at LBL. In 1975, radiotherapy using neon ions was started. Since these pioneering studies at LBL, use of charged particle radiotherapy has spread all over the world. In Japan, proton radiotherapy and carbon ion radiotherapy were started at the National Institute of Radiological Sciences (NIRS) in 1979 and 1994, respectively, and there are now 6 facilities for charged particle radiotherapy in operation in the country.

2.1. Characteristics of charged particle radiotherapy

When high energy charged particles enter a material, their deposited energy will gradually increase with penetrating depth, giving rise to a sharp maximum (Bragg peak) near the end of the range. A small angle deflection of the charged particles leads to their spreading away from the incident trajectory in passing through the materials. The degree of the deflection of the high energy charged particles used in radiotherapy is much smaller than that of electrons. Hence, high energy charged particles offer excellent conditions for a highly conformal treatment of malignant tumors due to these favorable physical properties.

Furthermore heavy charged particles, carbon ions for example, also show favorable radiobiological characteristics. Heavy charged particles can sterilize cells more effectively than photons or protons. Heavy charged particles are able to suppress recovery from radiation injury, the oxygen effect and cell cycle dependence due to radio-sensitivity. Due to their biological effectiveness, the charged particles heavier than protons are expected to be effective towards radiation resistant tumors.

2.2. Energies of the charged particles for radiotherapy

A 3 cm range is required for the treatment of eye melanoma or superficially located tumors. For the treatment of deep seated tumors, a 30 cm range is required. In order to realize these ranges in a human body, it is necessary to have energies from 50 MeV to 250 MeV for proton therapy and from 50 MeV per nucleon to 1000 MeV per nucleon for heavy charged particles.

3. Materials and Methods

Two review tasks were done.

1. We collected the information from representative foreign facilities for charged particle radiotherapy concerning to radiation protection at each facility.

2. We checked the necessity for legal controls regarding safety practices of charged particle radiotherapy based on an experimental investigation of radiation levels around several Japanese treatment facilities.

4. Results and Discussion

4.1. Trends in international regulations for proton and heavy ion therapies

Proton and carbon ion particle radiotherapy institutes in Europe, South Africa and the USA were visited and their situations regarding government regulations were detailed through interviews with staff members in charge of radiation protection. Basic data were also obtained. Dose and exposure limits etc. in the therapy institutions are based on the ICRP (International Commission on Radiological Protection) recommendations, except in the USA where they are based on the NCRP (National Council on Radiation Protection and Measurements) recommendations. There are no specific regulations for charged particle radiotherapy institutes, and the regulations for X-rays and electrons of current medical accelerators have been applied.

The situations in representative facilities in five countries are summarized below. Our survey identified no items that should be added to the Japanese regulatory system.

4.1.1 Germany

Carbon Ion Therapy Institute: Gesellschaft für Schwerionenforschung mbH (GSI)
Under construction: German Cancer Research Center (KDFZ)

In Germany, regulatory laws on radiation protection have been made by the federal government, and local governments regulate each institute. The laws include medical matters, and there are specific guidelines on medicines. Details of the radiation protection items are described in the regulations. Dose limits for person and places basically follow ICRP recommendations, so they are similar to those of Japan. However, some points such as the boundary of a controlled area are more severe than in Japan.

Since the method used in the GSI is Raster Scanning, and it will be used also in the KDFZ, the amounts of activated materials produced are very small. The activation levels of patients are extremely low, so that specific protective actions are not done after irradiation for patients, their urine and their belongings. The activation levels of air in the therapy room are very low, and only ordinary ventilation is used. The exposure doses of medical staff members are measured every month and have been lower than the detection limit (under 0.1mSv) for the last several years of operation of a radiotherapy institute.

4.1.2. USA

Proton Therapy Institute:

Proton Treatment and Research Center, Loma Linda University Medical Center, The University of Florida Proton Therapy Institute

Under construction at the time of the survey, but therapy has now been started:

Proton Therapy Center, University of Texas MD Anderson Cancer Center

The total number of patients which have been treated at Loma Linda University Medical Center is the largest of any facility in the USA. The MD Anderson Proton Treatment and Research Center is one of the latest proton therapy institutes in the world.

In the USA, laws and regulations are made by the state governments independently. Loma Linda University, MD Anderson Cancer Center and The University of Florida, therefore, are regulated by the laws of California*, Texas** and Florida***, respectively. However, the fundamental standpoint of radiation protection is based mainly on NCRP Report Nos. 49, 51 and 144. The regulations for proton therapy institutes are not so different from those for medical accelerators or other general radiation protection regulations. Many neutron therapies have ever been performed in MD Anderson hospital. The risk of activation in proton therapy has not been considered because the activation levels are quite lower compared to those in neutron therapy.

There are no special guidelines for proton therapy because of the low activation levels of patients and other materials. For activated materials in the therapy room, they can be removed from the room after checking that the activated level is as low as the background level.

4.1.3. Sweden

Proton Therapy Institute: Uppsala University

In Sweden, there are double regulatory bodies; a national ministry in general charge and the Swedish Radiation Protection Authority (SSI) which is a special agency handling radiation protection. Detailed regulations are performed by the SSI which also makes regulatory inspections and issues licenses for therapy etc. In addition, changes in therapy institutes and radiation incidences and accidents are reported to SSI. Basically, regarding regulations for proton therapy institutes, there are no differences from general radiation protection regulations. Actual measurements are regarded as the methods for the dose estimations of the ambient condition of the institutes and periodic measurements are not needed if there are no changes within the institutes or irradiation methods. Specific guidelines have not been made because the activation levels of the patients or materials on proton therapy are very low.

4.1.4. Switzerland

Proton Therapy Institute: The PSI Proton Therapy Facility

The PSI Proton Therapy Facility, which has performed proton therapy with its own original technique, has no special regulations for particle therapy; rather it follows the common regulations of other accelerator facilities. This is for the same reason as noted above: the activation levels of the patients or materials are very low. The regulatory authority for particle therapy facilities is the Ministry of Health, which verifies the safety of shielding, equipment and machines, and inspects the facilities irregularly. The current regulations are based on those for linac devices; however, PSI facility has prepared its own more strict regulations.

4.1.5. Republic of South Africa

Proton Therapy Institute: iThemba Therapy Facility

The iThemba Therapy Facility has performed both proton and neutron therapies. The

* Joint Commission Acceptance of Health Care Organization: California 17 Radiation Control Regulations

** Department of State Health Service of Texas: Radiation Safety Requirements for Accelerators, Therapeutic Radiation Machine and Simulators (Effective October 1, 2000)

*** FAC-64E-5: Florida Administrative Code: Rules of the State of Florida, Dept. of Health, Chapter 64E-5, Control of Radiation Hazard Regulations

fundamental viewpoint for radiation protection and related values such as dose limits are mainly based on the ICRP recommendations. Attention has been paid to activation of shielding materials by neutrons. However, there are no special standards for radiation protection. The regulations are the same as for linac devices etc.

4.2. Estimation of exposure to radiation workers from activated materials

4.2.1. Aim of the study

Charged particle radiotherapy facilities in Japan are equipped with an interlock system that hinders any persons (except the patient) from entering or staying in the irradiation room during a therapeutic irradiation. The system is intended to protect patient's families or facility workers such as radiation oncologists, radiation technologists, nurses, medical physicists and so on, from being directly irradiated by the therapeutic beam. However, due to their relativistic high energy, the therapeutic beams cause nuclear reactions when passing through matter and various kinds of unstable (radioactive) isotopes are produced along the beam path. As a consequence of the decay of the isotopes, some induced radioactivity remains in the irradiation room for a certain period after the irradiation. Among radiation workers, radiation technologists are considered to suffer the highest level of exposure from the induced radioactivity because they must enter the irradiation room to execute necessary tasks immediately after the end of the therapeutic irradiation.

In this study, the practical maximum doses to be received by the radiation technologists were assessed based on measurements of the induced radioactivity at several particle radiotherapy facilities in Japan.

4.2.2. Devices of interest

The induced radioactivity was measured for the following therapy-related devices: a multi-leaf collimator, a patient collimator and a patient compensator. The multi-leaf collimator occupies the end of a series of stationary irradiation devices collectively called the irradiation nozzle. The latter two devices are removable and attached next to the multi-leaf collimator for the therapeutic irradiation. The irradiation target in the patient's body is positioned just downstream from the patient compensator.

4.2.2.1. Multi-leaf collimator

The multi-leaf collimator (MLC) is built into the irradiation nozzle. The MLC consists of a stack of many thin, layered metal plates. The lateral position of each layer is independently adjustable via remote control according to the situations of individual patients. The outline of the irradiation field is defined as the aperture bordered by the metal layers. Facilities not equipped with the MLC substitute a block collimator which can take the same role. The block collimator has one or two pairs of opposing metal blocks which allow rough shaping of the irradiation field edge.

4.2.2.2. Patient collimator

The patient collimator is used to precisely match the shape of the irradiation field with the planned shape. The collimator is made of a metal block with an aperture that corresponds to the shape of the target in the patient. The patient collimator protects normal tissues surrounding the target from unwanted dose exposure. Brass is commonly preferred as the material due to its easy machining property. A patient collimator is prepared for each port. After the therapeutic irradiation, it is detached from

the irradiation nozzle.

4.2.2.3. Patient compensator (bolus)

The patient compensator is used in order to match the range end of the therapeutic beam in the patient with the distal shape of the target. The incident beam stops at a shallower point in the body if the beam passes through a thicker patient compensator before entering the body. A patient collimator is also prepared for each port and detached from the nozzle after the therapeutic irradiation. Polyethylene is widely used due to its similarity to human soft tissues in terms of density.

4.2.2.4. Tissue substitute

In order to assess the radioactivity induced in the patient body, a commercially available tissue substitute, Tough Water Phantom was used. The phantom was 300 mm thick and the center of the phantom was positioned at the isocenter in the irradiation room.

4.2.3. Measuring instrument

Ion chamber survey meters were used for the measurements. This device allows measurements of 1cm dose equivalent in the photon field. Skin surface dose is also measurable in the photon field and β-rays can be measured by removing a build-up cap from the ion chamber entrance window. All survey meters used in this study were calibrated within one year prior to measurements in a reference field that has kept traceability to the Japanese national standard.

4.2.4. Experiments

Incident energies of the beam were chosen from among each facility's available energy set to have approximately 250 mm range in water for protons or 150 mm (and 250 mm, if available) for carbon ions. As a typical therapeutic beam, the beam was broadened about 150 mm in diameter in the lateral direction, and spread out 60 mm in water in the axial direction. A physical dose of 5 Gy was given to the center of the spread-out Bragg peak (SOBP) in each irradiation. The experimental conditions for devices of each facility are specified below.

4.2.4.1. Multi-leaf collimator

A rectangular aperture of 50 mm width and height was formed at the center of the irradiation field by the MLC. The 1 cm dose equivalent rate was measured every 30 s at two positions: one was on, or as close as possible to the downstream surface of the collimator, and the other was 500 mm downstream from the collimator surface to the effective center of the survey meter. The measurements were done by attaching or detaching the build-up cap in order to separate the contribution from photons and β-rays. Unless otherwise specified, the experimental conditions were always the same in the following cases.

4.2.4.2. Patient collimator

The same aperture as for the MLC, a rectangular shape of 50 mm width and height, was machined at the center of the metal block. Immediately after the irradiation, the 1 cm dose equivalent rate was measured *in situ* on the downstream surface of the collimator and 300 mm downstream from the collimator surface. The collimator was removed and taken to a place where the background dose is low, e.g. the treatment room. In order to avoid the background contribution, the irradiated collimator was successively detached from the irradiation nozzle; then the 1 cm dose equivalent rates were measured every 30 s on the upstream surface of the collimator and 300 mm upstream from the surface. By doing these measurements outside of the irradiation room, the

background level was negligible and could be avoided.

4.2.4.3. *Patient compensator*

A rectangular unmachined block, made of the same material as the patient compensator, was used. The block thickness was equivalent to 100 mm of water in terms of the beam range. Immediately after the irradiation, the 1cm dose equivalent dose was measured *in situ* on the downstream surface of the block as well as 300 mm downstream from the block surface. Just as for the patient collimator, the block was detached from the irradiation nozzle; then every 30 s the 1cm dose equivalent rates on the upstream surface of the collimator and 300 mm upstream from the surface were measured outside of the irradiation room in order to avoid the background contribution.

4.2.4.4. *Tissue substitute*

In the irradiation of the Tough Water Phantom, the other previously mentioned devices were retracted in order to produce the maximum radioactivity in the phantom. Then, the edge of the irradiation field was shaped with another patient collimator having a 100 mm× 100 mm rectangular aperture in order to simulate irradiation of a large size tumor.

Like the above cases, the 1 cm dose equivalent rates were measured *in situ* on the downstream surface of the block as well as 300 mm downstream from the block surface immediately after the irradiation. The phantom was taken from the irradiation room; then every 30 s the 1 cm dose equivalent rates on the upstream surface of the collimator and 300 mm upstream from the surface were measured outside of the irradiation room in order to avoid the background contribution.

4.2.5. *Data analysis*

The time series change of the measured 1 cm dose equivalent rate was well fitted with a summation of two exponential functions.

$$\dot{H}=p_1e^{-t/p_2}+p_3e^{-t/p_4} \quad (1)$$

$\dot{H}$: 1 cm dose equivalent rate [μSv/h]

t: elapsed time after the end of the irradiation [h]

p_1, p_3: fitting parameters related to intensity [μSv/h]

p_2, p_4: fitting parameters related to decay constant [h]

Eq. (1) shows the decay of two radioisotopes with different decay constants. The parameters p_2 and p_4 correspond to the decay constant. When a worker completes a task between t_1 and t_2 after the end of the irradiation, the dose equivalent received by the worker is given by the following integral.

$$\begin{aligned} H &= \int_{t_1}^{t_2} \dot{H}dt = \int_{t_1}^{t_2} (p_1e^{-t/p_2}+p_3e^{-t/p_4})dt \\ &= p_1p_2(e^{-t_1/p_2}-e^{-t_2/p_2}) \\ &\quad + p_3p_4(e^{-t_1/p_4}-e^{-t_2/p_4}) \end{aligned} \quad (2)$$

4.2.6. *Estimation of exposure dose*

The dose equivalent to the radiation technologists was estimated. Here, the sequential process starting with detaching the devices from the nozzle is assumed to be executed by just one radiation technologist in order to estimate the maximum dose. Table 1 summarizes the processes considered.

At first, effective dose by photons from the MLC received when detaching a patient-fixation device was derived as an integral of Eq. (2) from t_1=25 [s] to t_2=55 [s] at 50 cm downstream from the MLC with the capped survey meter. Similarly, those from the patient collimator (denoted as the collimator) and the pa-